Research article

Experimental study on the strain energy evolution mechanism of thick and hard sandstone roof in Xinjiang Mining Area

Dongdong Qin [a], Zechao Chang [b,*,1], Ze Xia [b]

[a] School of Mines, Shanxi Institute of Technology, Yangquan, Shanxi, 045000, China
[b] School of Mines, China University of Mining and Technology, Xuzhou, Jiangsu, 221116, China

A B S T R A C T

For understanding the mechanical performance and strain energy evolution mechanism of thick hard roof sandstone samples, a sequence of uniaxial compression trials with acoustic emission (AE) monitoring were carried out. The results indicate: (1) The stress-strain curve of the thick hard roof sandstone specimens exhibits distinct stage characteristics. Based on the evolvement of instantaneous axial stiffness, it is separated into Fracture Closure Phase, Elastic Deformation Phase, Steady Fracture Expansion Phase, Unsteady Fracture Expansion Phase, and Post-Peak Phase. (2) The AE energy and cumulative count curves of the thick hard roof sandstone specimens also exhibit significant stage characteristics and can be mutually corroborated with the stage division of the stress-strain curve. (3) Based on the energy conservation principle, the evolution of strain energy density in the thick hard roof sandstone specimens under uniaxial compression loading was analyzed, and plastic strain energy increment was employed to study the stage characteristics of strain energy dissipation. (4) A damage constitutive model for the thick hard roof sandstone specimens was constructed, considering the characteristics of strain energy dissipation. This model effectively describes the stress-strain relationship among the samples, which undergo strain hardening, strain softening, and sudden destruction.

1. Introduction

The sudden extensive fracture and collapse of a hard roof pose one of the main threats to the safety of coal mining operations [1–4]. However, as coal resource extraction gradually moves from shallow depths to deeper underground spaces, mining production is increasingly affected by complex geological environments such as high in-situ stress, high geothermal temperatures, high pore pressures, and strong excavation disturbances. This results in a remarkable growth in the elastic strain energy accumulation in the hard roof, indicating a higher danger of dynamic hazards like rock bursts and coal and gas outbursts [5–8].

Rock damage is the process of development, propagation, aggregation, connection and penetration of initial cracks in rock. Because AE is highly sensitive to the generation and propagation of cracks in materials and structures, AE technology finds extensive applications in areas such as material damage detection [9]. Zhang et al. [10] monitored AE energy release and AE event locations during uniaxial compression tests of coal, concrete, and concrete-confined coal samples, investigating the development process and spatio-temporal distribution of micro-fractures inside coal samples during the loading process. Wang et al. [11]observed impact,

ringing and energy characteristics of fracture-induced acoustic emission signals under true triaxial compression in granite, studying the close connection between acoustic emission signals and rock deformation. Dong et al. [12]combined monitoring data from 18 AE sensors to explore variation characteristics of AE signals during the elastic-plastic stage of granite samples under uniaxial compression, pointing out that the rate of acoustic emission events and wave velocity serve as effective monitoring parameters for rock instability. Kong et al. [13], based on acoustic emission counting and cumulative count evolution, qualitatively explained internal crack evolution in coal samples during loading and proposed a damage variable for coal samples derived from acoustic emission counts, quantitatively analyzing damage evolution in these samples.

In addition, the process of internal damage and fracturing in rock is a process of dissipating energy [14]. The occurrence and severity of rockbursts are closely related to the processes of storing, dissipating and releasing energy within rock mass. It is evident that the accumulation and dissipation of strain energy within the hard roof are critical factors leading to the accumulation of damage, instability, and the triggering of complex dynamic disasters in coal and rock formations [15,16]. Many scholars have conducted research on the relationship between rock failure and elastic strain energy. Ai et al. [17] proposed a brittleness evaluation index that can describe the transition from absolute plasticity to absolute brittleness in rocks from an energy perspective based on the evolution of strain energy during uniaxial compression. Zhang et al. [18] investigated the true triaxial compression of three types of hard rocks using indicators such as energy storing limits, strain energy ratios and transition rates. They pointed out that the mineral composition and microstructure of rocks contribute remarkably to strain energy development. Yang et al. [19], through theoretical analysis, examined the rock mechanical behaviour and studied the transformation and distribution of elastic strain energy in the course of fracture extension. Characteristics of energy evolution during brittle damage in hard rocks were revealed from both elastic strain energy and surface energy. Du et al. [20] suggested that two energy-based indicators, peak strength strain energy storing indicator and residual elastic energy indicator, can accurately reflect the energy and rockburst tendency of hard rocks from both elastic energy storage and residual elastic energy. Therefore, studying the accumulation and dissipation of strain energy within the hard roof and its relationship with the damage evolution process is of significant importance for monitoring the stability of surrounding rock masses, deformation control, and disaster early warning in deep earth engineering projects [21,22].

Apart from experimental research, scholars both domestically and internationally have studied the destruction evolvement laws of rock materials on the basis of continuous failure mechanics and statistical theories. Liu et al. [23] brought in destruction variables on the basis of dissipative energy and established a damage constitutive model on the basis of rock energy evolution to describe rock damage. According to the relationship among stress-strain behavior, AE modes, and energy evolvement features during triaxial compression experiments on coal samples, Ning et al. [24] presented a new approach for fracture initiation and propagation threshold determination based on energy evolution processes. Gong et al. [25] carried out a sequence of uniaxial compression and single-cycle load and unload trials on weakly cemented coal, lean coal, gas coal, anthracite, and gas-bearing coal. They proposed a coal burst tendency evaluation method on the basis of residual elastic energy indicators.

This paper conducted uniaxial compression tests on sandstone samples from a thick hard roof in a mine in Xinjiang, China. The primary focus was to investigate the stress-strain behaviour of these samples during axial compression. Additionally, the AE monitoring technology was utilized to analyze the evolutionary characteristics of AE energy and cumulative counts in the compression process. It also delved into the stage-wise characteristics of the damage process during loading. In the end, on the basis of the energy balance relation of the samples, the characteristics of damage evolution were analyzed and a constitutive model for injury evolvement on the basis of strain energy was established.

2. Experiment pre-processing

2.1. Sample preparation

The rock samples employed for the experiments were taken from the roof of a thick hard sandstone stratum in the Zhundong Mining
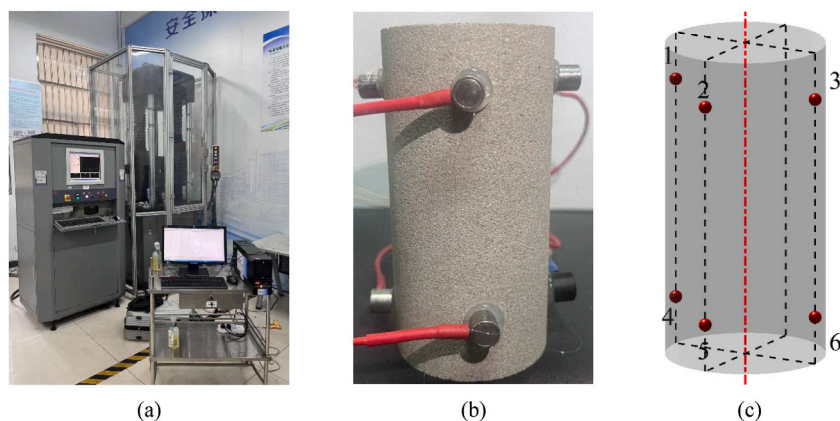

Fig. 1. (a) Instruments and equipment. (b) Prepared specimen. (c)Arrangement of AE sensors.

Area of Xinjiang, China. The workface is approximately 450 m deep on average. According to the core drilling records, the thickness of the thick hard sandstone roof, composed of fine sandstone, measures 17.5 m. After extraction, the thick hard roof sandstone samples were sealed with plastic wrap and transported in foam-padded wooden crates to preserve their initial structure and moisture content. Following the guidelines outlined in GB/T 50266–2013 "Standard Methods for Engineering Rock Mass Testing", the extracted rock specimens were manufactured into cylinder, measuring φ50 mm × 100 mm. The dimensional error of the rock samples did not exceed 0.03 mm, the unevenness of both end faces was within 0.05 mm, and the deviation of the end faces from the axis was not over 0.25°.

2.2. Experimental instruments and equipment

Fig. 1(a) illustrates the primary testing equipment and monitoring system for the uniaxial compression tests on the thick hard roof sandstone specimens. Uniaxial compression testing of composite specimens was carried out using an American hydraulic servo universal test machine, which had a maximum axial loading capacity of 1000 kN and a frame stiffness of 100 kN/mm, with a loading accuracy of ±0.03 %. Simultaneously, an AE monitoring system (PCI-2, Physical Acoustic Corporation, America) was employed for monitoring AE events during compression. The AE system was configured with a capture threshold of 40 dB, a yield of 40 dB, and a sample frequency of 2 MHz. The AE sensors used (NANA-30, Physical Acoustic Corporation, America) had a working frequency scope of 125–750 kHz, with a resonant frequency at 140 kHz. The acoustic emission sensor arrangement is as shown Fig. 1(b and c).

2.3. Experimental procedure

Uniaxial compression tests on thick hard roof sandstone specimens were carried out employing displacement controlling loading method, and the speed was 0.2 mm/min. Simultaneously, six Nano30 sensors were symmetrically positioned on the surface of the thick hard roof sandstone specimens. Fig. 1(b) presents the layout of the AE sensors. To mitigate the influence of end effects on the experimental process, a layer of approximately 2 mm thick Vaseline was uniformly applied between the spherical hinge and the specimen as a lubricant.

3. Experiment outcomes and analysis

3.1. Stress–strain behaviour

Fig. 2(a–d) displays the uniaxial compression stress-strain curves of the thick hard roof sandstone samples. The paper also divides the stages of rock damage based on the evolutionary characteristics of instantaneous axial stiffness. Note that instantaneous axial stiffness was obtained using dynamic point regression analysis. In this method, the instantaneous axial stiffness values were calculated as the slope of the fitted lines of the data points in the sliding sampling windows, and both the sampling window and sliding step were set to 100 data points [26].
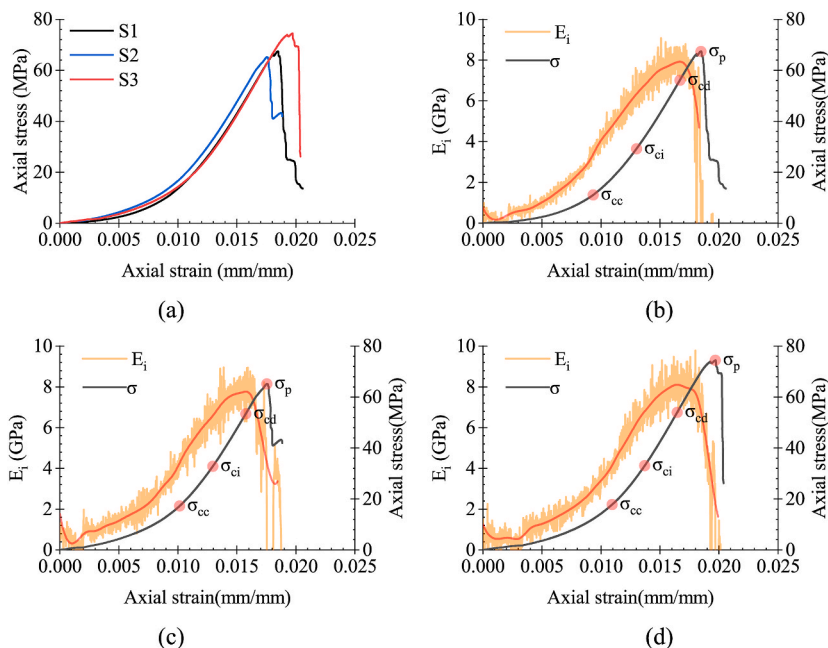

Fig. 2. Stress–strain curves of samples: (a) stress–strain curves of group; (b) stress–strain curves and deformation modulus curve of specimen S1; (c) stress–strain curves and deformation modulus curve of specimen S2; (d) stress–strain curves and deformation modulus curve of specimen S3.

Fig. 2(a–d) indicates that the stress-strain behavior of the thick hard roof sandstone sample exhibits a single strain hardening or softening characteristic during distinct phases. However, the instantaneous axial stiffness-stress curve of the rock sample shows local fluctuations. This is because the inherent heterogeneity of natural rock samples is difficult to avoid at the microscopic level: the elastic deformation of the rock matrix or the partial squeezing of microcracks leads to local strain hardening, while the initiation and propagation of some microcracks result in local strain softening. The macroscopic mechanical behavior of the rock sample is an outcome of these two mechanisms balancing each other microscopically. Therefore, based on the evolutionary characteristics of the instantaneous axial stiffness, the uniaxial compression process of the rock sample is separated into 5 phases.

1. Fracture Closure Phase (OA): The stress-strain behaviour of the rock specimen is during this phase until the axial loading reaches the fracture closure stress (σ_{cc}). The stress-strain curve exhibits a non-linear concave upward trend under low uniaxial stress, and the original microcracks within the sample gradually close. However, the load-bearing structure of the sample is optimized, and the instantaneous axial stiffness increases exponentially in response to axial strain.

2. Elastic Deformation Phase (AB): While the axial load reaches the fracture initiation stress (σ_{cc}), the stress-strain behavior of the rock specimen moves into this phase. The stress-strain curve exhibits approximately linear growth, and the load-bearing structure of the sample remains intact, undergoing recoverable deformation. However, as the original pores continue to compress, the load-bearing structure of the rock specimen further optimizes, and the stress-strain curve shows non-linear hardening behavior. The instantaneous axial stiffness continues to increase, and the rate of increase gradually rises.

3. Steady Fracture Extension Phase (BC): While the axial load reaches the sample cracking stress (σ_{ci}), the stress-strain behavior of the rock specimen moves into the stable crack extension phase. The stress-strain curve maintains approximately linear growth, but the original microcracks inside the rock sample begin to extend and initiate new microcracks. The destruction of the rock specimen begins to increase, and the instantaneous axial stiffness still maintains an upward trend, but the rate of increase decreases significantly.

4. Unsteady Fracture Extension Phase (CD): While the axial load achieves the sample damage stress (σ_{cd}), the stress-strain behaviour of the rock sample enters the unsteady fracture extension stage. Microcracks inside the rock sample propagate and expand, forming macroscopic cracks, resulting in a dramatic growth in destruction to the rock sample. Strain softening occurs, and the stress-strain curve exhibits a non-linear upward concave trend. The instantaneous axial stiffness shows a decreasing trend.

5. Post-Peak Phase (D-): While the axial load achieves the sample post-peak stress (σp), the stress-strain behavior of the rock specimen moves into this phase. Macroscopic cracks inside the rock continue to expand, further damaging the load-bearing construction of the rock specimen, even leading to direct failure. The load-bearing capacity of the sample continues to decline.

To further analyze the mechanical performance evolvement during the damage process of the thick hard roof sandstone samples, an analysis of stress thresholds and strain thresholds was conducted (see Table 1). As shown in Fig. 3(a, b), the peak strains (ε_p) for S1–S3 specimens are 0.0185, 0.0175, and 0.0197, correspondingly, with an average peak strain ($\overline{\varepsilon_p}$) of 0.0186. The peak stresses (σ_p) for S1–S3 samples are 67.39 MPa, 65.16 MPa, and 74.42 MPa, correspondingly, and the average peak stress ($\overline{\sigma_p}$) is 68.99 MPa. The crack closure strains (ε_{cc}) for S1–S3 samples are 0.0093, 0.010, and 0.0110, respectively, with an average crack closure strain ($\overline{\varepsilon_{cc}}$) of 0.0101, reaching 54.67 % of ($\overline{\varepsilon_p}$). The crack closure stresses (σ_{cc}) for S1–S3 samples are 11.07 MPa, 17.23 MPa, and 17.83 MPa, respectively, with an average crack closure stress ($\overline{\sigma_{cc}}$) of 15.37 MPa, which is only 22.29 % of ($\overline{\sigma_p}$). The crack initiation strains (ε_{ci}) for S1–S3 samples are 0.0130, 0.0130, and 0.0137, respectively, with an average crack initiation strain ($\overline{\varepsilon_{ci}}$) of 0.0132, reaching 71.24 % of ($\overline{\varepsilon_p}$). The crack initiation stresses (σ_{ci}) for S1–S3 samples are 29.22 MPa, 32.80 MPa, and 33.08 MPa, correspondingly, and the average crack initiation stress ($\overline{\sigma_{ci}}$) is 31.70 MPa, which is an increase to 45.95 % of ($\overline{\sigma_p}$). The damage strains (ε_{cd}) for S1–S3 samples are 0.0167, 0.0158, and 0.0165, respectively, with an average damage strain ($\overline{\varepsilon_{cd}}$) of 0.0163, reaching 87.82 % of ($\overline{\varepsilon_p}$). The damage stresses (σ_{cd}) for S1–S3 samples are 56.10 MPa, 53.48 MPa, and 54.04 MPa, correspondingly, and the average damage stress ($\overline{\sigma_{cd}}$) is 54.54 MPa, increasing to 79.05 % of ($\overline{\sigma_p}$). It can be observed that in the early stages of sample damage, axial strain increases rapidly while axial stress increases relatively slowly. During the later stages, the increase rates of axial strain slow down, while the increase rates of axial stress significantly rise.

3.2. AE response

Fig. 4(a–c) illustrates the stress, AE energy and cumulative count curves in the course of the uniaxial compression of the thick hard roof sandstone sample. Using the damage threshold as a reference, it can be observed that the AE response of the sample exhibits distinct stages. Taking S2 as a typical sample for analysis:

Table 1
Characteristic stresses and strains of samples.

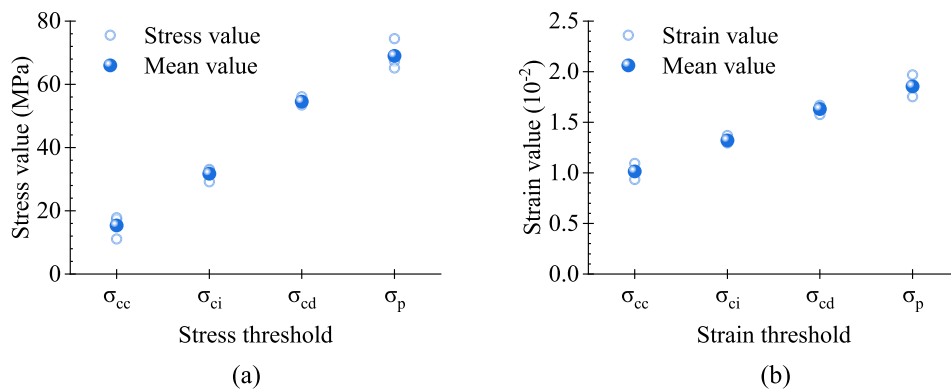| No.	ε_{cc} /10^{-2}	σ_{cc} /MPa	ε_{ci} /10^{-2}	σ_{ci} /MPa	ε_{cd} /10^{-2}	σ_{cd} /MPa	ε_f /10^{-2}	σ_f /MPa
S1	0.93	11.07	1.30	29.22	1.67	56.10	1.85	67.39
S2	1.02	17.23	1.30	32.80	1.58	53.48	1.75	65.16
S3	1.10	17.83	1.37	33.08	1.65	54.04	1.97	74.42

Fig. 3. Damage threshold of samples based on (a) Stress and (b) strain.

(1) During early loading phases, AE signals are primarily induced by the closure and compaction of numerous pre-existing cracks within the sample. Therefore, during this stage, AE energy remains stable at a low level, and the accumulative AE count shows a slow growth.
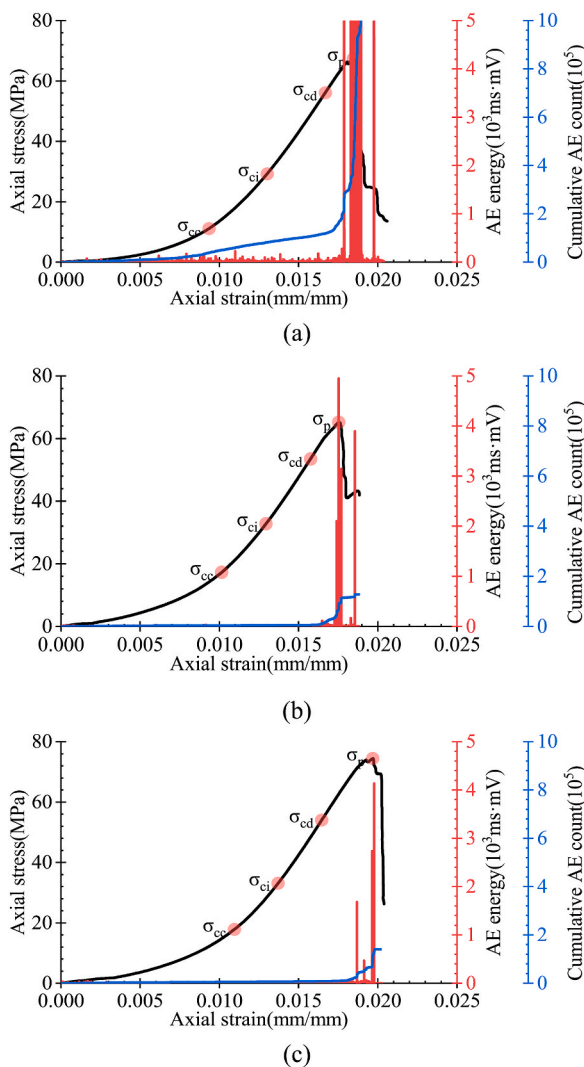

Fig. 4. AE characteristics of sample (a) S1, (b) S2 and (c)S3.

(2) Upon entering the elastic deformation stage, external loading is insufficient to initiate the formation of new microcracks. AE signals are mainly induced by further compaction and frictional behavior within the closed cracks of the sample. This leads to AE energy remaining stable at a low level in this stage, but the rate of cumulative AE count growth significantly decreases.

(3) As the sample enters the stage of stable crack propagation, the pre-existing microcracks inside the sample begin to propagate, and new microcracks initiate. The AE energy curve shows a substantial increase, and the cumulative AE count starts to accelerate.

(4) During the subsequent phase of stable fracture propagation, the pre-existing microcracks inside the sample continue to propagate, and new microcracks initiate. The AE energy curve rises significantly, and the cumulative AE count begins to accelerate.

(5) When the sample enters the stage of unstable crack propagation, as microcracks further develop and connect with macroscopic cracks, the mechanical performance of the specimen deteriorates obviously. AE activity becomes active, and AE signals increase significantly both in number and in energy. The cumulative AE count exhibits an exponential growth trend.

Overall, the specimen shows relatively quiet AE activity during fracture closure phase elastic deformation phase and steady fracture extension phase, with very low energy release in AE signals. During the unsteady fracture extension phase and post-peak phase, the AE activity is more active, with a relatively higher energy release in the acoustic emission signals. Moreover, AE activity is highly correlated with stress drop. Before a significant stress drop occurs, the AE energy curve shows low-level fluctuations, and the accumulative AE count shows a slow growth. After a significant stress drop, the AE energy increases substantially, and the accumulative AE count suddenly increases. This is because during the process of stress drop, the elastic strain energy are released along with the expansion of cracks. The greater the stress drop, the more rapid and significant the crack expansion, inducing more active AE signals and generating more AE energy.

4. Discussion

4.1. Strain energy evolution

During the loading process, the sample undergoes energy input, storing, dissipation, and releasing. The testing equipment, through external loading, introduces energy into the sample. This energy is partitioned into different forms: a portion of it is stored as elastic strain energy, another portion slowly dissipates in the process of promoting internal fracture progression within the sample, and the remaining part is emitted as thermal energy, electromagnetic radiation energy, and AE energy [27]. Therefore, based on the thermodynamic principles, the total strain energy (U) in specimen deformation failure is related to elastic strain energy (U^e), plastic strain energy (U^d), and release energy (U^r) as follows [28,29]:

$$U = U^e + U^d + U^r \tag{1}$$

However, for natural sandstone samples, U^r is much smaller than U. Therefore, the plastic strain energy of the sample is calculated using U and U^e [30,31]:

$$U^d = U - U^e \tag{2}$$

U and U^e can be represented in the principal stress space as follows [32]:

$$U = \int \sigma_1 d\varepsilon_1 + \int \sigma_2 d\varepsilon_2 + \int \sigma_3 d\varepsilon_3 \tag{3}$$

$$U^e = \frac{1}{2}\left(\sigma_1 \varepsilon_1^e + \sigma_2 \varepsilon_2^e + \sigma_3 \varepsilon_3^e\right) \tag{4}$$

where, σ_i represents the three principal stresses, ε_i is the three-dimensional strain, and ε_i^e represents the three-dimensional elastic strain.

Considering that only the axial stress σ_1 performs work on specimen during uniaxial compression testing, Eqs. (3) and (4) can be simplified as follows:

$$U = \int \sigma_1 d\varepsilon_1 \tag{5}$$

$$U^e = \frac{1}{2}\sigma_1 \varepsilon_1^e = \frac{1}{2E}\sigma_1^2 \tag{6}$$

where, E represents the elastic modulus of the sample.

Fig. 5(a–c) displays the evolvement curve of the strain energy for a typical sample. Before reaching the peak stress, as the axial stress increases, the extent of microcrack closure in the sample increases, the stiffness increases, and the input energy required to drive the sample to undergo unit strain increases. U exhibits a nonlinear concave evolution characteristic. After reaching the peak stress, macroscopic cracks cause a rapid deterioration of the load-bearing structure of the sample, the stiffness decreases, and the input energy required to drive the sample to undergo unit strain decreases. U exhibits a nonlinear convex evolution characteristic. Using the damage

threshold as a reference, it can be observed that the evolution curves of U^e and U^d are roughly separated into 5 phases. (1) During the crack closure phase, there are many microcracks inside the sample that have not yet closed. The stiffness of the sample is relatively low, and the input energy is mainly dissipated during the process of driving the closure of microcracks. U^d closely matches the U evolution curve, and U^e remains close to zero. (2) When moving into the elastic deformation phase, the main microcracks inside the sample are closed, forming a load-bearing structure together with the sample matrix. The input energy is primarily saved as elastic strain energy. U^e increases rapidly, and its evolution curve quickly approaches the U evolution curve. The U^d curve remains relatively stable. (3) During the steady fracture propagation phase, the core load-bearing structure of the sample remains unchanged, but microcracks inside the core of the sample begin to rapidly nucleate and develop. The stiffness of the sample begins to decrease. Therefore, both U^e and U^d show a rising tendency. The increase speed of U^d progressively increases, while it decreases progressively for U^e. (4) In the non-stable crack propagation stage, microcracks inside the sample intersect to form macroscopic cracks, leading to the rapid release and redistribution of stress inside the sample. As a result, the growth rate of U^e significantly decreases, while the growth rate of U^d significantly increases. (5) During the post-peak phase, upon reaching the peak stress, the specimen hits its energy storing limits, and macroscopic cracks penetrate the sample, causing it to fail. A large amount of U^e is converted into U^d.

The statistical characteristics of U_c, U_c^e, and U^d correspond to the stress thresholds σ_{cc}, σ_{ci}, σ_{cd}, and σ_p are presented in Table 2. As shown in Fig. 6, for the thick hard roof sandstone samples, the average U^e, U^d and U corresponding to σcc are 15.62 kJ/m³, 35.10 kJ/m³, and 50.72 kJ/m³, respectively. When the axial stress of the thick hard roof sandstone samples reaches σ_{ci}, the average U^e, U^d and U increase to 64.12 kJ/m³, 55.99 kJ/m³, and 120.11 kJ/m³, separately, increasing by 310.41 %, 59.53 %, and 136.81 %, separately, in comparison with the end of the previous damage stage. When the axial stress of the thick hard roof sandstone samples reaches σ_{cd}, the average U^e, U^d and U increase to 189.25 kJ/m³, 62.41 kJ/m³, and 251.66 kJ/m³, respectively, which is an increase of 195.14 %, 11.47 %, and 109.53 % in comparison with the termination of previous damage phase. When the axial stress of the thick hard roof sandstone samples reaches σ_p, the average U^e, U^d and U increase to 302.46 kJ/m³, 92.93 kJ/m³, and 395.39 kJ/m³, respectively, representing an increase of 59.82 %, 48.89 %, and 57.11 % compared to the end of the previous damage stage.

To further discuss the evolution of strain energy in the course of stress-strain, the concept of plastic strain energy increment is introduced to characterize the energy dissipation within any loading step. This parameter is calculated based on the formula below:

$$\Delta U^d(\text{t}) = U^d(t + \Delta t) - U^d(t) \tag{7}$$

where, $\Delta U^d(\text{t})$ represents the increment in plastic strain energy, $U^d(t)$ represents the plastic strain energy at time t, and Δt represents the time interval.

Fig. 7(a–c) depicts the evolution of the plastic strain energy increment with axial strain during the compression test, with a magnified view on the right side. As can be seen, the plastic strain energy increment shows distinct stages. Using the damage threshold as a reference point, the evolution of the strain energy increment is separated into the below five phases. (1) During the crack closure phase (OA), the growth in plastic strain energy is induced by the closure and compaction of pre-existing microcracks inside the thick and hard sandstone specimen, resulting in a gradual increase in the plastic strain energy increment. (2) Upon entering the elastic stage
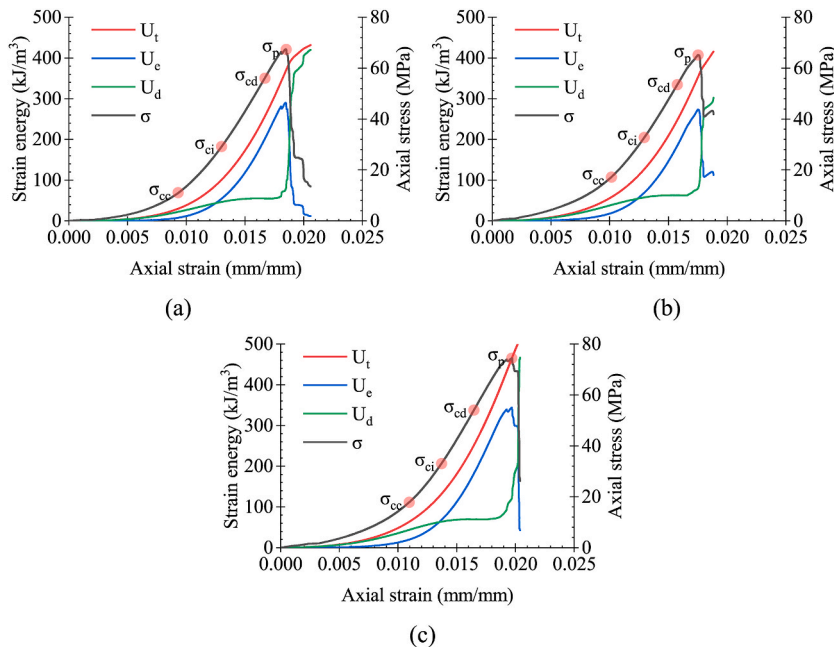

Fig. 5. Energy evolution curves of sample (a) S1, (b) S2 and (c)S3.

Table 2
Characteristic strain energy of coal samples.

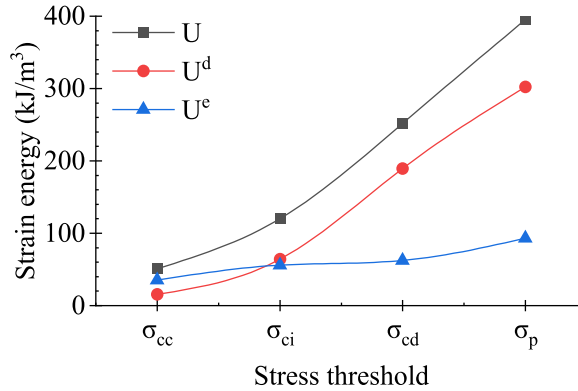| Strain energy	No.	σ_{cc}	σ_{ci}	σ_{cd}	σ_p
U (kJ/m3)	S1	30.33	101.29	256.3	367.63
	S2	58.35	127.05	247.36	354.07
	S3	63.48	131.99	251.33	464.46
U^e (kJ/m3)	S1	7.86	54.71	201.34	289.96
	S2	19.19	69.46	184.52	273.11
	S3	19.82	68.19	181.88	344.3
U^d (kJ/m3)	S1	22.48	46.59	54.96	77.67
	S2	39.16	57.59	62.83	80.96
	S3	43.66	63.8	69.45	120.16

Fig. 6. Characteristic strain energy of samples.

(AB), as the axial stress level increases, further compression and closure of microcracks inside the thick and hard sandstone specimen occur. However, the increment in plastic strain energy reaches a relatively stable state. (3) After entering the stage of stable crack propagation (BC), microcracks within the thick and hard sandstone specimen continue to develop and expand. The opening of microcracks gradually becomes dominant, leading to another slow increase in the plastic strain energy increment. (4) Upon entering the stage of unstable crack propagation (CD), microcracks inside the thick and hard sandstone specimen interconnect, forming macroscopic cracks. This results in the rapid release and redistribution of internal stresses within the specimen. Simultaneously, the plastic strain energy increment begins to experience a significant increase. (5) When the rock specimen reaches its peak stress (D-), almost complete penetration of macroscopic cracks reduces the load-carrying capacity of the specimen, causing the plastic strain energy increment to exhibit an overall decreasing trend, except for several instances of sharp increases.

4.2. Damage evolution

As described earlier, dissipative energy is primarily employed for driving the initiation and development of microcracks within the specimen, thereby promoting irreversible damage to the sample. On the other hand, elastic strain energy is primarily utilized for facilitating elastic deformation within the specimen, which recovers with the release of elastic strain energy as the load is removed. To quantitatively study the development of damage during rock deformation and failure processes, the proportions of elastic strain energy and dissipative strain energy to absorptive energy during any load condition are determined as the elastic strain energy proportion (P_e) and the dissipative strain energy proportion (P_d), respectively. These ratios serve as indicators of the intactness and degree of damage in the specimen.

As shown in Fig. 8(a–c), during the specimen's failure process, P_e and P_d exhibit strong regularities. Due to the presence of natural defects within the specimen, in the early stages of loading, the absorptive energy in specimen is mainly transformed into dissipative energy through promoting the closure of natural microcracks, resulting in an initially high level of P_d (approximately 0.97), while P_e is only around 0.03. With the gradual growth of axial strain, P_e progressively rises while P_d decreases, reflecting the optimization of the load-bearing structure because of the progressive closure of inherent cracks during loading. When the specimen reaches the vicinity of σ_{cd}, P_e reaches its peak and gradually decreases, while P_d begins to steadily increase. This indicates that the strain softening induced by the evolution of microcracks inside the rock begins to dominate in a balance with strain hardening induced by the closure of microcracks. When the specimen reaches the peak stress, P_d on the strain curve jumps to nearly 1, while P_e undergoes a sharp drop to nearly 0.
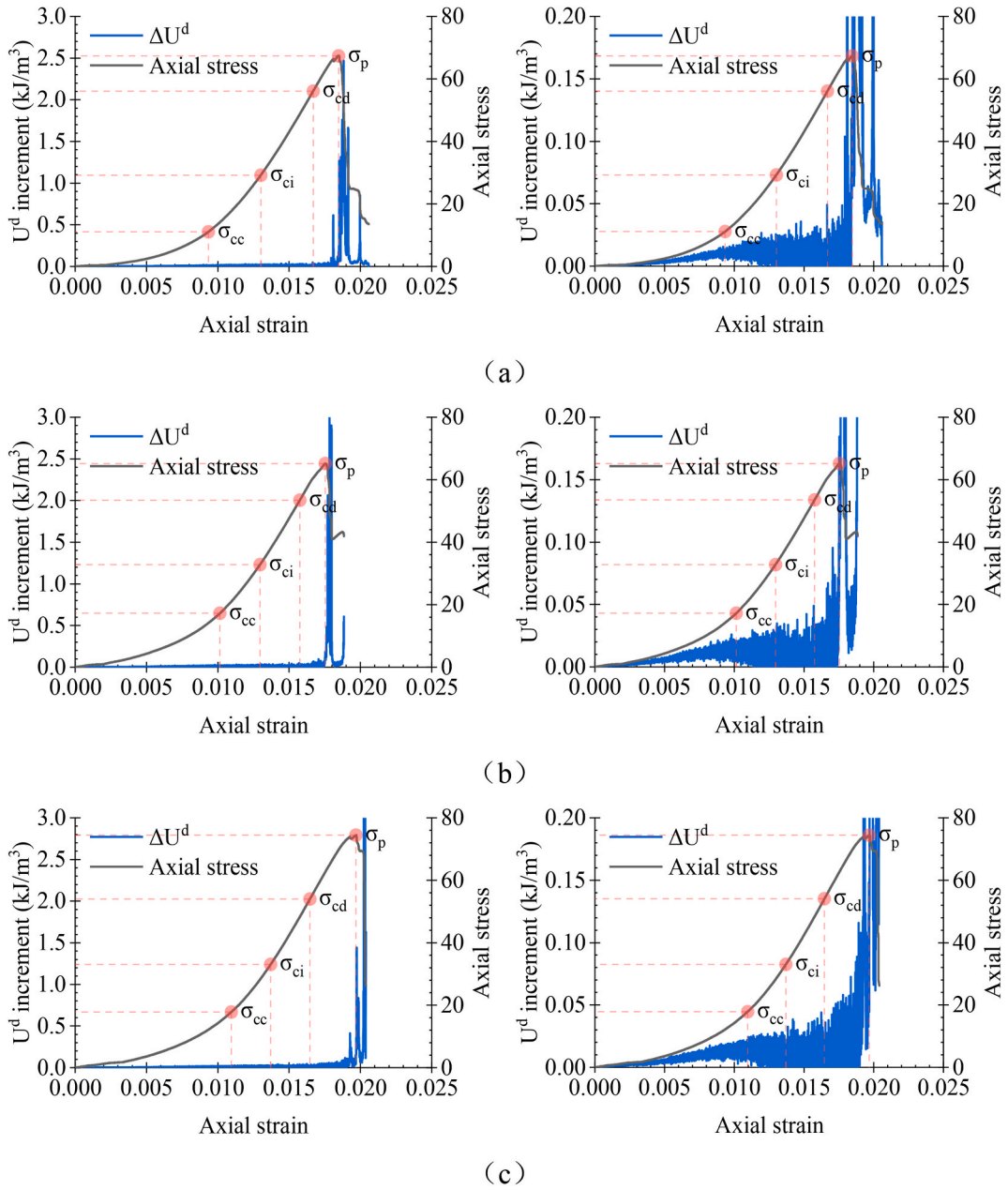
Fig. 7. Plastic strain energy increment evolution curves of sample (a) S1, (b) S2 and (c)S3.

4.3. Damage constitutive model

On the basis of the inherent relation between specimen strain energy evolvement and specimen damage development, this paper defines P_d as the specimen damage variable:

$$D = 1 - \exp\left(-P_d / P_f\right), \tag{8}$$

where D represents the degree of damage, while P_f signifies the average value of P_d. P_f was ascertain with the assumption that the critical injury state, denoted as D_f, corresponds to complete damage. In practical terms, this is represented by the endpoint on the curve where P_d is considered the critical dissipative strain energy proportion (P_{df}). Consequently, P_f is calculated by substituting D_f and P_{df}:

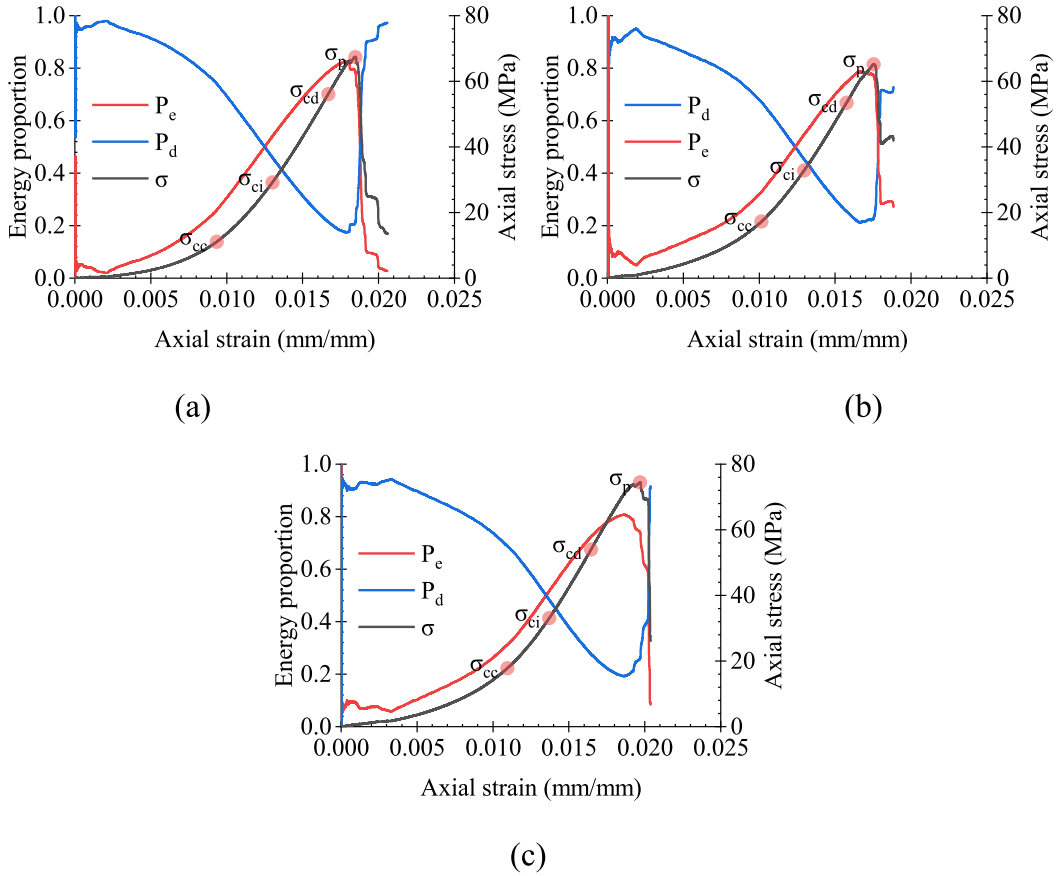$$P_f = \frac{-P_{df}}{\ln\left(1 - D_f\right)}, \tag{9}$$

Fig. 8. Evolution curves of P_e and P_d of sample (a) S1, (b) S2 and (c)S3.

where D_f represents the discrepancy between the critical and minimum values of the dissipative energy proportion.

On the basis of the theory of continuous damage mechanics, the stress-strain behaviour of the specimen can be described as follows [33]:

$$\sigma_1 = (1 - D)E_0\varepsilon_1, \tag{10}$$

The stress-strain curves fitted using the damage constitutive model are shown in Fig. 9(**a–c**). The fitted stress-strain curves display nonlinearity and concave upward tendency during initial load phase and nonlinearity and concave downward trends in the later loading phase, which closely resemble the strain hardening and strain softening features observed in the tests. Consequently, the damage constitutive model on the basis of dissipated energy appears to be capable of effectively describing the stress-strain relation of the thick and hard roof sandstone specimens subjected to uniaxial compression loading.

5. Conclusion

During the research, uniaxial compression experiments were performed on thick hard roof sandstone specimens from a coal mine in Xinjiang Mining Area, with AE monitoring. The following are the key conclusions drawn from the mechanical performance analysis, AE count and energy characteristics, and the strain energy-based damage evolution under different confinement conditions:

1. The uniaxial compression tests performed on thick hard roof sandstone specimens unveiled a stress-strain behavior characterized by distinct and identifiable stages. These stages were categorized as Fracture Closure Phase, Elastic Deformation Phase, Steady Fracture Expansion Phase, Unsteady Fracture Expansion Phase, and Post-Peak Phase. Furthermore, the curves depicting the AE energy and accumulative counts demonstrated analogous stage-specific features and exhibited a robust correlation with the stage division in the stress-strain curve. These findings underscore the importance of utilizing instantaneous axial stiffness as a valuable tool for gaining in-depth insights into the mechanical response of these specimens.
2. The study utilized the energy conservation theory to investigate the evolution of strain energy density during uniaxial compression loading. Furthermore, the plastic strain energy increment was introduced to characterize in detail the stage-specific of strain energy dissipation. The observed correlation between the strain energy-strain curve and the AE energy evolution curve reveals similar
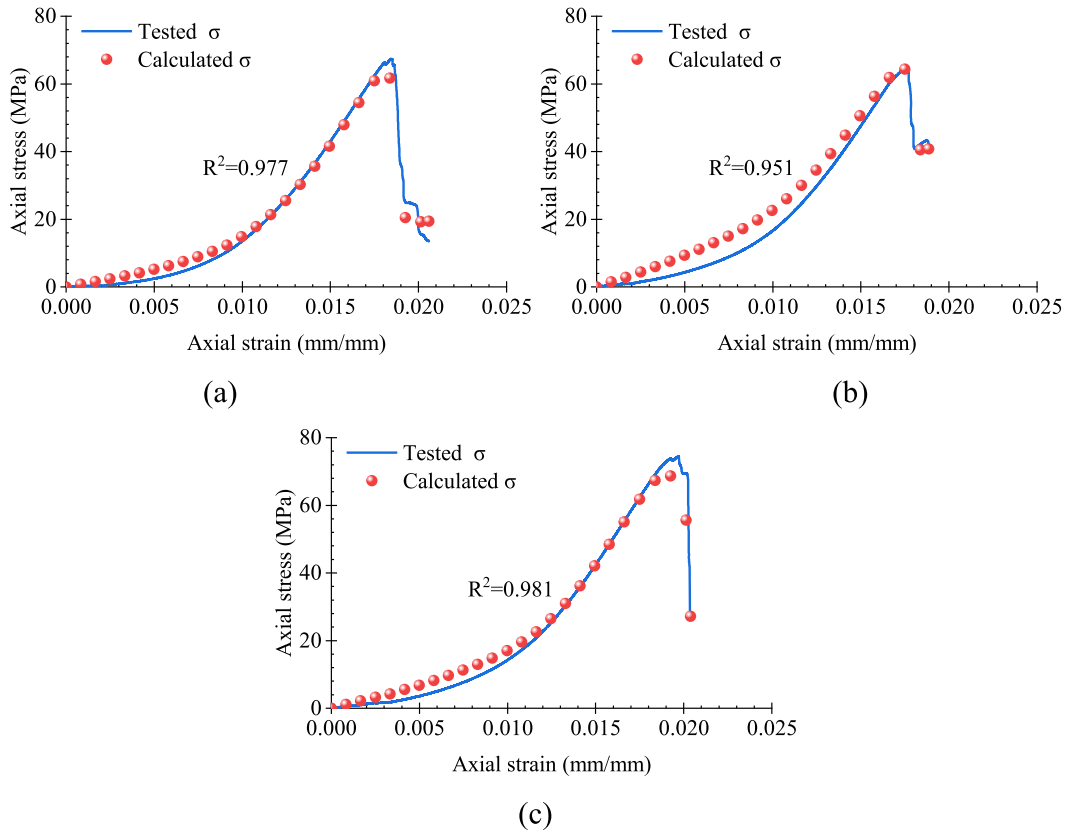
Fig. 9. Comparison between theoretical and experimental curves of sample (a) S1, (b) S2 and (c)S3.

developmental trends and stage-specific characteristics. These findings facilitate better comprehension about the mechanical behavior and strain energy evolution of the tested specimens, shedding light on their damage mechanisms and structural responses during compression loading.

3. According to the intrinsic relationship between strain energy evolvement and damage development, the dissipative strain energy proportion was brought in as a damage variable. After the loading initiation, P_d exhibited a gradual decrease - gradual increase - abrupt rise trend, reflecting respectively the strain softening due to the closure of numerous natural defects in the samples, strain softening resulting from the extensive development of microcracks, and the sudden failure caused by the macroscopic fracture penetrating the specimen. A damage constitutive model was developed to account for the strain energy dissipation characteristics observed in the thick hard roof sandstone specimens. This model effectively captures the complete stress-strain relationship, including stages of strain hardening, strain softening, and sudden failure.

Data availability statement

Data will be made available on request.

CRediT authorship contribution statement

Dongdong Qin: Writing – original draft, Methodology, Investigation, Funding acquisition. **Zechao Chang:** Writing – original draft, Project administration, Investigation, Formal analysis. **Ze Xia:** Writing – review & editing, Methodology, Investigation, Data curation.

Declaration of competing interest

The authors declare that they have no known competing financial interests or personal relationships that could have appeared to influence the work reported in this paper.

Acknowledgments

References

[1] M. Yu, J. Zuo, J. Sun, C. Mi, Z. Li, Investigation on fracture models and ground pressure distribution of thick hard rock strata including weak interlayer, Int. J. Min. Sci. Technol. 32 (1) (2022) 137–153, https://doi.org/10.1016/j.ijmst.2021.10.009.

[2] C. Lu, G. Liu, Y. Liu, N. Zhang, J. Xue, L. Zhang, Microseismic multi-parameter characteristics of rockburst hazard induced by hard roof fall and high stress concentration, Int. J. Rock Mech. Min. Sci. 76 (2015) 18–32, https://doi.org/10.1016/j.ijrmms.2015.02.005.

[3] Y. Lu, T. Gong, B. Xia, B. Yu, F. Huang, Target stratum determination of surface hydraulic fracturing for far-field hard roof control in underground extra-thick coal extraction: a case study, Rock Mech. Rock Eng. 52 (8) (2019) 2725–2740, https://doi.org/10.1007/s00603-018-1616-9.

[4] Z. Tong, L. Changyou, K. Yetilmezsoy, Z. Baisheng, Z. Shuai, Fractural structure of thick hard roof stratum using long beam theory and numerical modeling, Environ. Earth Sci. 76 (21) (2017) 1–13, https://doi.org/10.1007/s12665-017-7103-x.

[5] G. Feng, P. Wang, Simulation of recovery of upper remnant coal pillar while mining the ultra-close lower panel using longwall top coal caving, Int. J. Min. Sci. Technol. 30 (1) (2020) 55–61, https://doi.org/10.1016/j.ijmst.2019.12.017.

[6] B. Huang, J. Liu, Q. Zhang, The reasonable breaking location of overhanging hard roof for directional hydraulic fracturing to control strong strata behaviors of gob-side entry, Int. J. Rock Mech. Min. Sci. 103 (2018) 1–11, https://doi.org/10.1016/j.ijrmms.2018.01.013.

[7] G. Wu, W. Yu, J. Zuo, S. Du, Experimental and theoretical investigation on mechanisms performance of the rock-coal-bolt (rcb) composite system, Int. J. Min. Sci. Technol. 30 (6) (2020) 759–768, https://doi.org/10.1016/j.ijmst.2020.08.002.

[8] T. Zhang, L. Yu, H. Su, Q. Zhang, S. Chai, Experimental and numerical investigations on the tensile mechanical behavior of marbles containing dynamic damage, Int. J. Min. Sci. Technol. 32 (1) (2022) 89–102, https://doi.org/10.1016/j.ijmst.2021.08.002.

[9] L. Dong, Y. Chen, D. Sun, Y. Zhang, S. Deng, Implications for identification of principal stress directions from acoustic emission characteristics of granite under biaxial compression experiments, J. Rock Mech. Geotech. Eng. 15 (4) (2023) 852–863, https://doi.org/10.1016/j.jrmge.2022.06.003.

[10] C. Zhang, Z. Jin, G. Feng, X. Song, G. Rui, Z. Yujiang, Double peaked stress–strain behavior and progressive failure mechanism of encased coal pillars under uniaxial compression, Rock Mech. Rock Eng. 53 (7) (2020) 3253–3266, https://doi.org/10.1007/s00603-020-02101-7.

[11] C. Wang, C. Cao, C. Li, X. Chuai, G. Zhao, H. Lu, Experimental investigation on synergetic prediction of granite rockburst using rock failure time and acoustic emission energy, J. Cent. South Univ. 29 (4) (2022) 1262–1273, https://doi.org/10.1007/s11771-022-4971-3.

[12] L. Dong, Y. Chen, D. Sun, Y. Zhang, Implications for rock instability precursors and principal stress direction from rock acoustic experiments, Int. J. Min. Sci. Technol. 31 (5) (2021) 789–798, https://doi.org/10.1016/j.ijmst.2021.06.006.

[13] X. Kong, E. Wang, X. He, E. Zhao, C. Zhao, Mechanical characteristics and dynamic damage evolution mechanism of coal samples in compressive loading experiments, Eng. Fract. Mech. 210 (2019) 160–169, https://doi.org/10.1016/j.engfracmech.2018.04.005.

[14] X. Feng, C. Yang, R. Kong, et al., Excavation-induced deep hard rock fracturing: methodology and applications, J. Rock Mech. Geotech. Eng. 14 (1) (2022) 1–34, https://doi.org/10.1016/j.jrmge.2021.12.003.

[15] X. Dong, G. Yang, S. Liu, Experimental study on ae response and damage evolution characteristics of frozen sandstone under uniaxial compression, Cold Reg. Sci. Technol. 193 (2022) 103424, https://doi.org/10.1016/j.coldregions.2021.103424.

[16] F. Gao, S. Cao, K. Zhou, Y. Lin, L. Zhu, Damage characteristics and energy-dissipation mechanism of frozen-thawed sandstone subjected to loading, Cold Reg. Sci. Technol. 169 (2020) 102920, https://doi.org/10.1016/j.coldregions.2019.102920.

[17] C. Ai, J. Zhang, Y. Li, J. Zeng, X. Yang, J. Wang, Estimation criteria for rock brittleness based on energy analysis during the rupturing process, Rock Mech. Rock Eng. 49 (12) (2016) 4681–4698, https://doi.org/10.1007/s00603-016-1078-x.

[18] Y. Zhang, X. Feng, X. Zhang, et al., Strain energy evolution characteristics and mechanisms of hard rocks under true triaxial compression, Eng. Geol. 260 (2019) 105222, https://doi.org/10.1016/j.enggeo.2019.105222.

[19] B. Yang, L. Xue, Y. Duan, Investigation into energy conversion and distribution during brittle failure of hard rock, Bull. Eng. Geol. Environ. 81 (3) (2022), https://doi.org/10.1007/s10064-022-02582-6.

[20] K. Du, X. Luo, S. Yang, J.A. Danial, J. Zhou, An insight from energy index characterization to determine the proneness of rockburst for hard rock, Geomech. Energy Environ. 35 (2023) 100478, https://doi.org/10.1016/j.gete.2023.100478.

[21] J. Gao, Z. Yu, L. Song, T. Wang, S. Wei, Durability of concrete exposed to sulfate attack under flexural loading and drying–wetting cycles, Construct. Build. Mater. 39 (2013) 33–38, https://doi.org/10.1016/j.conbuildmat.2012.05.033.

[22] B. Huang, J. Liu, The effect of loading rate on the behavior of samples composed of coal and rock, Int. J. Rock Mech. Min. Sci. 61 (2013) 23–30, https://doi.org/10.1016/j.ijrmms.2013.02.002.

[23] X.S. Liu, J.G. Ning, Y.L. Tan, Q.H. Gu, Damage constitutive model based on energy dissipation for intact rock subjected to cyclic loading, Int. J. Rock Mech. Min. Sci. 85 (2016) 27–32, https://doi.org/10.1016/j.ijrmms.2016.03.003.

[24] J. Ning, J. Wang, J. Jiang, S. Hu, L. Jiang, X. Liu, Estimation of crack initiation and propagation thresholds of confined brittle coal specimens based on energy dissipation theory, Rock Mech. Rock Eng. 51 (1) (2018) 119–134, https://doi.org/10.1007/s00603-017-1317-9.

[25] F. Gong, Y. Wang, Z. Wang, J. Pan, S. Luo, A new criterion of coal burst proneness based on the residual elastic energy index, Int. J. Min. Sci. Technol. 31 (4) (2021) 553–563, https://doi.org/10.1016/j.ijmst.2021.04.001.

[26] E. Eberhardt, D. Stead, B. Stimpson, R.S. Read, Identifying crack initiation and propagation thresholds in brittle rock, Can. Geotech. J. 35 (2) (1998) 222–233, https://doi.org/10.1139/t97-091.

[27] J. Wang, Z. Wang, S. Yang, A coupled macro- and meso-mechanical model for heterogeneous coal, Int. J. Rock Mech. Min. Sci. 94 (2017) 64–81, https://doi.org/10.1016/j.ijrmms.2017.03.002.

[28] W. Cai, X. Bai, G. Si, W. Cao, S. Gong, L. Dou, A monitoring investigation into rock burst mechanism based on the coupled theory of static and dynamic stresses, Rock Mech. Rock Eng. 53 (12) (2020) 5451–5471, https://doi.org/10.1007/s00603-020-02237-6.

[29] W. Cai, L. Dou, G. Si, et al., A new seismic-based strain energy methodology for coal burst forecasting in underground coal mines, Int. J. Rock Mech. Min. Sci. 123 (2019) 104086, https://doi.org/10.1016/j.ijrmms.2019.104086.

[30] Z. Chen, C. He, D. Wu, G. Xu, W. Yang, Fracture evolution and energy mechanism of deep-buried carbonaceous slate, Acta Geotech 12 (6) (2017) 1243–1260, https://doi.org/10.1007/s11440-017-0606-5.

[31] J. Kim, K. Lee, W. Cho, H. Choi, G. Cho, A comparative evaluation of stress–strain and acoustic emission methods for quantitative damage assessments of brittle rock, Rock Mech. Rock Eng. 48 (2) (2015) 495–508, https://doi.org/10.1007/s00603-014-0590-0.

[32] R. Peng, Y. Ju, J.G. Wang, H. Xie, F. Gao, L. Mao, Energy dissipation and release during coal failure under conventional triaxial compression, Rock Mech. Rock Eng. 48 (2) (2015) 509–526, https://doi.org/10.1007/s00603-014-0602-0.

[33] X. Li, W. Cao, Y. Su, A statistical damage constitutive model for softening behavior of rocks, Eng. Geol. 143–144 (2012) 1–17, https://doi.org/10.1016/j.enggeo.2012.05.005.